



1 **Improvement of OMI ozone profile retrievals by**
2 **simultaneously fitting Polar Mesospheric Clouds**

3

4 **Juseon Bak¹ (sunnypark@pusan.ac.kr), Xiong Liu² (xliu@cfa.harvard.edu), Jae H. Kim¹**
5 **(jaekim@pusan.ac.kr), Matthew T. Deland³ (matthew.deland@ssaihq.com), Kelly Chance²**
6 **(kchance@cfa.harvard.edu)**

7

8 *1 Pusan National University, Department of Atmospheric Sciences, Busan, South*
9 *Korea.*

10 *2 Harvard-Smithsonian Center for Astrophysics, Cambridge, MA, United States.*

11 *3 Systems and Applications, Inc. (SSAI), 10210 Greenbelt Rd., Suite 600, Lanham,*
12 *MD 20706, USA*

13

14

Abstract

15 The presence of polar mesospheric clouds (PMCs) in summer high latitudes could
16 affect the retrieval of ozone profiles using backscattered ultraviolet (UV) measurements.
17 PMC-induced errors in ozone profile retrievals from Ozone Monitoring Instrument (OMI)
18 backscattered UV measurements are investigated through comparisons with Microwave
19 Limb Sounder (MLS) ozone measurements. This comparison demonstrates that the
20 presence of PMCs leads to systematic biases at pressures less than 6 hPa (~35 km); the
21 biases increase from ~-2% at 2 hPa to ~-20% at 0.5 hPa on average, and are significantly
22 correlated with brightness of PMCs. Sensitivity studies show that the radiance sensitivity
23 to PMCs strongly depends on wavelength, increasing by a factor of ~4 from 300 nm to
24 265 nm. It also strongly depends on the PMC scattering, thus depending on viewing
25 geometry. The optimal estimation-based retrieval sensitivity analysis shows that PMCs
26 located at 80-85 km have the greatest effect on ozone retrievals at ~0.2 hPa (~60 km),



27 where the retrieval errors range from -2.5% with PMC optical depth (POD) of 10^{-4} to -
28 20% with 10^{-3} at back scattering angles, and the impacts increase by a factor of ~ 5 at
29 forward scattering angles due to stronger PMC sensitivities. To reduce the interference of
30 PMCs on ozone retrievals, we perform simultaneous retrievals of POD and ozone with a
31 loose constraint of 10^{-3} for POD, which results in retrieval errors of $1 - 4 \times 10^{-4}$. It
32 is demonstrated that the negative bias of OMI ozone retrievals relative to MLS can be
33 improved by including the PMC in the forward model calculation and retrieval.

34 1 Introduction

35 PMCs are tenuous layers of ice crystals that form at 80-85 km altitude only during
36 the hemispheric summer season (~ 30 days before to ~ 65 days after summer solstice) at
37 high latitudes and occasionally at mid-latitudes (Thomas et al., 1991; Taylor et al., 2002;
38 DeLand et al., 2010). It has been suggested that the change of PMC properties such as
39 frequency and brightness is linked to long-term changes in the composition and thermal
40 structure of our atmosphere caused by human activities.

41 The mesospheric clouds in the daytime are detectable only from space, whereas
42 ground-based observations are limited to immediately after sunset or before sunrise
43 (DeLand et al., 2003). The optimal way to observe PMC from space is to employ limb-
44 viewing sensors measuring the scattered solar radiation from which the cloud layers are
45 easily identified as the enhanced radiances against the relatively weak atmospheric
46 scattering (Thomas et al., 1991; Deland et al., 2006). The seasonal-latitudinal behaviors
47 of PMC occurrence, brightness, altitude were characterized from various limb-viewing
48 instruments including the Solar Mesosphere Explorer (SME), the Student nitric Oxide
49 Explore (SNOE), and the SCanning Imaging Absorption spectroMeter for Atmospheric
50 CHartographY (Olivero and Thomas, 1986; Bailey et al., 2005; von Savigny et al., 2004).
51 These satellite measurements further contribute to understanding of microphysical
52 properties of PMCs such as water vapor content, size distribution, and shape, which still



53 remain a challenge (e.g., Thomas, 1984; Rapp et al., 2007; von Savigny and Burrows,
54 2007).

55 Even through nadir-viewing sensors could not provide information about the PMC
56 altitude, Thomas et al. (1991) first demonstrated that PMCs are detectable from nadir-
57 looking UV measurements using a brightness-based detection algorithm. PMC
58 occurrence and residual albedo have been derived from Solar Backscatter Ultraviolet
59 (SBUV, SBUV/2) and Ozone Monitoring Instrument (OMI) nadir UV measurements at
60 shorter wavelengths below 300 nm where the Rayleigh-scattered background is
61 comparatively low due to very strong ozone absorption. Thomas et al. (1991) found an
62 anti-correlation of the PMC occurrence frequency with solar activity from 8 years of
63 SBUV albedo data over the period 1978 to 1986. Further studies have demonstrated
64 long-term trends over 30+ years in PMC occurrence frequency, brightness, particle radii,
65 and ice water content (DeLand et al., 2003, 2007; Shettle et al., 2009; Hervig and
66 Stevens, 2014; DeLand and Thomas, 2015). OMI PMC observations were used to
67 characterize the local time variation of PMC occurrence frequency and brightness, with
68 the advantage of overlapping pixels over the polar region due to the wide swath of OMI
69 (DeLand et al., 2011). On the other hand, the detectability of the signal of PMCs from UV
70 wavelengths below 300 nm in the ozone Hartley bands implies that failure to account for
71 PMCs in ozone profile retrievals using these wavelengths might affect the determination
72 of ozone and its trends in the upper atmosphere from nadir-viewing UV instruments such
73 as SBUV, SBUV/2, OMI, Global Ozone Monitoring Experiment (GOME) (ESA, 1995),
74 SCIAMACHY, GOME-2 (Munro et al., 2006), and Ozone Mapping and Profiler Suite
75 (OMPS) Nadir Profiler instruments (Flynn et al., 2014). However, the impact of PMCs
76 on ozone retrievals has not been taken into account for any ozone algorithm or even
77 thoroughly investigated with sufficient statistical data.

78 This paper is motivated by two main goals. The first objective is to quantify the effect
79 of PMCs on the current ozone profile retrievals from OMI measurements. For this



80 purpose, we combine the OMI PMC detection algorithm of DeLand et al. (2010) and the
81 OMI ozone profile retrieval algorithm of Liu et al. (2010a) and evaluate OMI ozone
82 profiles for PMC and non-PMC pixels through comparison with collocated MLS
83 measurements. The second one is to simultaneously retrieve the PMC optical depth with
84 ozone using an optimal estimation technique, to reduce the interference on ozone profile
85 retrievals.

86 In Sect. 2 we briefly introduce satellite measurements of OMI and MLS used in this
87 study and then describe the PMC detection algorithm and the PMC optical depth (POD)
88 retrieval algorithm, respectively. In Sect. 3.1 we evaluate OMI ozone profile retrievals
89 (without POD retrievals) against MLS ozone profiles during the PMC season. Section
90 3.2 presents the results from a retrieval sensitivity study to see if OMI measurements
91 provide adequate sensitivity to measure the PMC optical depth. The improvement of
92 ozone profile retrievals with simultaneously retrieved POD is discussed in Sect. 3.3. We
93 summarize and conclude our results in Sect. 4.

94 **2 Data and Methods**

95 **2.1 OMI and MLS Ozone measurements**

96 Both the OMI and MLS instruments are on board the NASA EOS Aura satellite
97 which is flown in a 705 km sun-synchronous polar orbit with ascending equator-crossing
98 time at ~13:45 (Schoeberl et al., 2006). MLS measurements are taken about 7 minutes
99 ahead of OMI for the same locations during daytime orbital tracks.

100 OMI is a nadir-viewing, ultraviolet-visible imaging spectrometer that measures
101 backscattered radiances from 260 to 500 nm (UV-1: 260-310 nm; UV-2: 310-365 nm;
102 VIS: 365-500 nm) at spectral resolutions of 0.42-0.63 nm with daily global coverage
103 (Levelt et al., 2006). The spatial resolution is $13 \times 24 \text{ km}^2$ for UV-2 and VIS and 13×48
104 km^2 for UV-1 at nadir position in the global mode. The OMI science teams provide two



105 operational total ozone products, OMTO3 (Bhartia and Wellemeyer, 2002) and
 106 OMDOAO3 (Veefkind et al., 2006), and one operational ozone profile product,
 107 OMO3PR (Kroon et al., 2011). We use the Smithsonian Astrophysical Observatory (SAO)
 108 ozone profile algorithm (Liu et al., 2010a) to deal with the error analysis of ozone profile
 109 retrievals due to PMC contamination. This algorithm retrieves partial column ozone at 24
 110 layers (surface to ~ 65 km) from OMI measurements with the fitting window of 270-330
 111 nm, based on the well-known optimal estimation (OE) technique (Rodgers, 2000). The
 112 iterative solution of the nonlinear problem is given as:

$$113 \quad X_{i+1} = X_i + (K_i^T S_y^{-1} K_i + S_a^{-1})^{-1} [K_i^T S_y^{-1} (Y - R(X_i)) - S_a^{-1} (X_i - X_a)] \quad (1)$$

114 where X_{i+1} , X_i , X_a , and Y are the current and previous state vectors, a priori vector,
 115 and measured radiance vector (defined as logarithm of normalized radiance), respectively.
 116 In order to improve fitting residuals, non-ozone parameters are included in the state
 117 vector such as BrO, surface albedo, wavelength shifts for radiance/irradiance and
 118 radiance/ozone cross sections and scaling parameters for the ring effect and mean fitting
 119 residuals. $R(X_i)$ and K_i are the simulated logarithm of radiance spectrum and the
 120 weighting function matrix ($\partial R / \partial X_i$) calculated using the Vector Linearized Discrete
 121 Ordinate Radiative Transfer model (VIDORT) (Spurr, 2006; 2008); the measurement
 122 error covariance matrix and a priori error covariance matrix are defined as S_y and S_a ,
 123 respectively. Ozone a priori information is generally taken from climatological mean
 124 values and standard deviations of long-term measurements data, respectively. This
 125 iterative process is performed until the cost function χ^2 (Eq. 2) converges.

$$126 \quad \chi^2 = \left\| S_y^{-\frac{1}{2}} \{K_i(X_{i+1} - X_i) - [Y - R(X_i)]\} \right\|_2^2 + \left\| S_a^{-\frac{1}{2}} (X_{i+1} - X_a) \right\|_2^2. \quad (2)$$

127 where $\| \cdot \|_2^2$ denote the the sum of each element squared.

128 The quality of the retrievals could be characterized by the solution error, defined as
 129 the root square sum of the random noise error and smoothing error. The vertical



130 resolution estimated by Liu et al. (2010a) is ~ 7-11 km in stratosphere. The retrieval
131 random-noise errors range from 1% in the middle stratosphere to 10% in the lower
132 stratosphere, and the solution errors are typically 1-6% in the stratosphere

133 MLS is a forward-looking, thermal-emission, microwave limb sounder that takes
134 measurements along-track and performs 240 limb scans per orbit with a footprint of ~ 6
135 km across-track and ~200 km along-track (Waters et al., 2006). The MLS ozone used
136 here is the version 4.2 standard ozone product (55 pressure levels) retrieved from the 240
137 GHz radiance information, publicly available from the NASA Goddard Space Flight
138 Center Earth Sciences (GES) data and Information Services Center (DISC). The typical
139 vertical resolution of this product is 2.5-3.5 km from 261 to 0.2 hPa and 4-5.5 km from
140 0.1 to 0.02 hPa; the precision is estimated to be a few% in the middle stratosphere, but 5-
141 100% below 150 hPa and 60-300% above 0.1 hPa. We apply all the data screening
142 criteria recommended in Livesey et al. (2015) and hence limit MLS ozone data to
143 “quality” higher than 1.0, “convergence” lower than 1.03, positive “*precision*” values and
144 even “status” value for the pressure range of 261-0.02 hPa.

145 Liu et al. (2010b) used the v2.2 MLS ozone data to validate the OMI ozone profile
146 retrievals and demonstrated the excellent OMI/MLS agreement of within 4% in the
147 middle stratosphere, except for positive biases of 5-10% above 0.5 hPa and negative
148 biases of 10-15% below 100 hPa, which are greatly improved by accounting for OMI’s
149 coarser vertical resolution using OMI averaging kernels.

150 **2.2 OMI PMC detection**

151 The flag data to detect both PMC and non-PMC regions from OMI measurements are
152 provided by DeLand et al. (2010). This detection algorithm uses albedo data ($A = I/F$, $I =$
153 radiance, $F =$ irradiance) at 267, 275, 283.5, 287.5, and 292.5 nm after interpolating all
154 spectra to a 0.5 nm grid and averaging three consecutive bins. The PMC pixels are
155 identified using enhancements above the Rayleigh scattering background. The



156 background atmospheric albedo due to Rayleigh scattering and ozone absorption (A_{ray}) is
157 determined using a 4th order fit in solar zenith angle to non-PMC pixels for each orbit,
158 after applying a geometric adjustment for cross-track albedo variations as defined in Eq.
159 (4) of DeLand et al. (2010). Positive signals of albedo residuals ($A - A_{\text{ray}}$) could be
160 induced by “false PMCs” including random instrument noise and geophysical variability
161 of ozone as well as by the PMC scattering. The minimum residual albedo value for PMC
162 detection is derived from measurements of clear atmospheric variability, and is adjusted
163 to eliminate false PMC signal due to instrument noise. The false PMC signal due to a
164 negative ozone deviation is screened out using the wavelength-dependence of PMC
165 signals that become stronger at shorter wavelengths. The PMC are typically observed at
166 latitudes above 55° from OMI where Solar Zenith Angle (SZA)s are above $\sim 35^\circ$,
167 Viewing Zenith Angle (VZA)s are below $\sim 70^\circ$, relative AZimuth Angle (AZA)s range
168 from $\sim 40^\circ$ to $\sim 80^\circ$ (right side of the nadir swath) and from $\sim 110^\circ$ and $\sim 130^\circ$ (left side
169 of the nadir swath), depending on the cross-track position.
170

171 2.3 PMC optical depth retrievals

172 In the standard ozone retrieval mode, the atmosphere is divided into 24 layers; the
173 bottom level of a layer i is defined as $P_i = 2^{\frac{(i-1)}{2}} \times 1013.15 \text{ hPa}$ with the top of
174 atmosphere, the upper level of layer 24, set at 0.087 hPa ($\sim 65 \text{ km}$). Radiance calculations
175 are made using the VLIDORT model for a Rayleigh atmosphere (no aerosol) assuming
176 Lambertian reflectance for ground surface and for clouds.

177 Due to the well-defined spatiotemporal range for PMCs, we will first detect PMCs
178 using the PMC detection algorithm specified in Sect. 2.2, and then calculate weighting
179 functions for POD and include them in the state vector with loose constraints. In the
180 POD retrieval mode, we add five more layers between $\sim 65 \text{ km}$ and ~ 90 at 5km intervals;



181 the bottom level of a layer i is defined as $P_i = 10^{-\left(\frac{(i-25) \times 5 + 65}{16}\right)} \times 1013.15$ for $i =$
182 25, ... 29. A PMC layer is inserted to the single layer of 80-85 km. Simulating the
183 scattering particles in the radiative process requires the specification of a particle size
184 distribution, the distribution size, and the distribution dispersion width, and a particle
185 shape. The primary component of the PMC particles was first confirmed as non-spherical
186 ice crystals by Hervig et al. (2001). The range of reported radii and size distribution
187 widths is 15-100 nm and 10-20 nm and log-normal or Gaussian size distributions are
188 normally assumed (Englert et al., 2007; Hervig et al., 2009). We assumed PMCs to be
189 spherical ice particles with a log-normal size distribution ($r_o = 55 \text{ nm}, \sigma_g = 1.4$), based
190 on the particle shape plays a minor role in the UV scattering (Baumgarten and Thomas,
191 2005; Eremenko et al., 2005); so we can derive extinction, single scattering albedo, and
192 phase function as a function of wavelength from Mie theory. The ice refractive index,
193 $1.33 + 5 \times 10^{-9}i$ at 300 nm from Warren (1984), was used for the entire wavelength range
194 because of low dependence on UV wavelength. The temperature profile is taken from
195 daily National Centers for Environmental Prediction (NCEP) final (FNL) Operational
196 Global analysis data (<http://rda.ucar.edu/datasets/ds083.2/>) below 10 hPa and from
197 climatological data above. We take ozone a priori information from monthly and zonal
198 mean ozone profile climatology presented in McPeters and Labow (2012), which is
199 based on the Aura MLS v3.3 data (2004-2010) and ozonesonde data (1988-2010).
200 Climatological a priori information for PMC optical thickness is not available. It is
201 selected here by trial and error. As a result, the a priori state and its error are set to be 0
202 and 10^{-3} , respectively. The initial POD value is taken to be 10^{-4} .

203 3 Results and Discussion

204 3.1 OMI /MLS comparison for with and without PMCs

205 The ozone profile comparisons between OMI without retrieving PMCs and MLS are



206 performed for two polar summer seasons, the North Hemisphere (NH), July 2007 and the
207 South Hemisphere (SH), January 2008 when the PMC occurrence is most frequent in a
208 given year. The comparison is limited to the high-latitude regions 75°N-85°N and 75°S-
209 85°S. The vertical range is limited to pressures larger than 0.1 hPa due to the weak
210 vertical ozone information from OMI measurements above; the retrieval could be
211 adequately resolved below ~0.5 hPa in the stratosphere based on the averaging kernels
212 (not shown here). In addition, MLS data have much larger uncertainties for ozone
213 retrievals above 0.1 hPa as mentioned in Sect. 2.1. The collocated OMI and MLS
214 measurements are separated into PMC and non-PMC pixels using the OMI PMC
215 detection flag specified in Sect. 2.2. In order to reduce the effect of the OMI smoothing
216 errors on the comparison, the high-resolution MLS data are convolved with the OMI
217 averaging kernels. The upper panels of figure 1 compare the OMI and MLS ozone
218 profiles averaged over PMC and non-PMC regions, respectively, on MLS pressure grids.
219 The mean original/smoothed MLS profiles show insignificant difference due to the
220 presence of PMCs, but the differences become significant for the mean OMI profiles in
221 the upper stratosphere. This demonstrates that the MLS stratospheric ozone product
222 could be a proper reference for the evaluation of OMI ozone retrievals during a PMC
223 season. Despite the large relative biases (~ -20 % at 0.5 hPa) due to the presence of
224 PMCs, the absolute bias is very small (~-0.05 DU at 0.5 hPa) because the ozone values in
225 upper layers are quite small (Figure 1 c and d). It implies that the effect of PMCs on total
226 ozone retrievals is negligible.

227 Figure 2 shows the mean biases and standard deviations of relative differences
228 between OMI and smoothed MLS ozone profiles. With non-PMC pixels the maximum
229 negative bias of OMI relative to MLS reaches -13% for the NH and -6% for the SH,
230 respectively, at ~0.5 hPa. This bias increases to -30% for the NH and -24% for the SH
231 when there are PMCs. The mean bias difference between PMC and non-PMC is the
232 difference between the black and green lines in Fig. 1, almost the same as the black line



233 since the MLS PMC/non-PMC difference is almost zero. We can see that the PMC effect
234 on OMI retrievals starts at ~6 hPa (~35 km), leading to erroneous ozone reductions of
235 ~20% at 0.5 hPa and ~2% at 2 hPa, similarly for both hemispheres. If we account for the
236 occurrence frequency of PMCs, the overall PMC effect on average ozone at 0.5 hPa is
237 7.1 % ($20 \% \times 2268/6388$) in the NH as there are ~ 2268 PMC pixels among 6388
238 pixels. This overall effect is three times larger compared to 2.3 % ($20 \% \times 792/6808$)
239 in the SH.

240 These PMC-induced ozone errors for OMI are more significant compared to ~10%
241 error in individual SBUV ozone retrievals based on the SBUV version 5 algorithm
242 (Thomas et al., 1991) and mean errors of up to 2-3 % in SBUV/2 ozone retrievals based
243 on the SBUV version 8.6 algorithm (Bhartia et al., 2013). That is because the OMI ozone
244 algorithm uses more wavelengths (270-330 nm) than SBUV algorithms (12 discrete
245 wavelength bands between 240 and 340 nm), which are sensitive at PMCs. The spatial
246 resolution of OMI, $48 \text{ km} \times 13 \text{ km}$ is much smaller than SBUV ($200 \text{ km} \times 200 \text{ km}$) and
247 SBUV/2 ($170 \text{ km} \times 170 \text{ km}$), so OMI has more chance to see a brighter PMC, resulting
248 in a larger impact on ozone retrievals. In addition, the comparison of standard deviations
249 shows almost no difference, indicating that the presence of PMCs mainly causes
250 systematic retrieval biases.

251 In Fig. 3, OMI/MLS biases are plotted as functions of the PMC albedo residuals at
252 267 nm for the NH polar summer. This figure emphasizes that brighter PMCs have
253 greater impact on the upper atmospheric ozone retrievals from UV measurements. The
254 OMI-MLS differences increase up to 60-80% at the topmost three layers when PMCs are
255 very bright. For dark PMC pixels, OMI retrievals agree well with MLS (mean biases are
256 close to zero), except for negative biases of -20% in 0.15-0.46 hPa and -10% in 0.68-1.0
257 hPa. Observations from the Cloud Imaging and Particle Size (CIPS) instrument on the
258 Aeronomy of Ice in the Mesosphere (AIM) satellite show that faint PMCs below the
259 OMI detection threshold, with brightness as low as $1.0 \times 10^{-6} \text{ sr}^{-1}$, are observed in 80-90%



260 of all samples at 80° latitude (Lumpe et al., 2013). Thus, even pixels that are “dark”
261 based on the OMI detection threshold may still have enough PMC contamination to bias
262 OMI ozone retrievals above 1.0 hPa. A strong negative correlation of more than 0.5 is
263 found in partial ozone columns above 2 hPa and no correlation (<0.1) at those layers
264 below 6 hPa. This similar behavior is detected for the relationship between biases due to
265 PMCs and albedo residuals in the SH polar summer presented in Table 1.

266

267 3.2 Sensitivity of UV radiances to PMCs

268 In Fig. 4.a, the sensitivity of OMI radiance to POD ranging from 10^{-5} to 10^{-3} is
269 plotted as functions of wavelength for a SZA of 70°, VZA of 45° and AZA of 135°.
270 Despite being optically thin, PMCs can significantly affect the UV radiances at shorter
271 wavelengths where the signal is weak, implying that the effect of PMC scattering may be
272 not negligible for the stratospheric ozone retrievals from OMI as well as the SBUV,
273 SBUV/2, GOME, GOME-2, SCIAMACHY, and OMPS Nadir Profiler instruments. The
274 presence of PMCs with the optical depth of 10^{-3} enhances the radiances from 2% at
275 300 nm to 8% at 265 nm for AZA of 135°. This sensitivity increases 4 times for the same
276 SZA and VZA but AZA of 45° (Fig. 4.b). Furthermore, it is shown that POD should be
277 larger than $\sim 10^{-4}$ for the case in Fig. 4.a and larger than $\sim 2 \times 10^{-5}$ in Fig. 4.b to be
278 detectable from UV measurements as the OMI measurement errors at ~ 270 nm are $\sim 1\%$.

279 Figure 4.c shows the viewing geometry dependence of PMC sensitivity at 267 nm.
280 The sensitivity varies largely with SZA, VZA, and AZA, except that at AZA larger than
281 90° the dependence on viewing geometry becomes relatively insignificant. This
282 dependence on AZA is mainly due to the steeper phase function variation of PMCs at
283 forward scattering angles, displayed in Fig. 4.d. The significant increase in PMC
284 sensitivity with larger SZA or VZA at $AZA < 90^\circ$ is mainly due to the larger photon path
285 length for PMC scattering. Overall, the dependence on viewing geometry is a direct



286 result of the strength of the PMC scattering.

287 Sensitivity studies using the optimal estimation formulation (with a loose PMC a
288 priori constraint of 10^{-3}) show that POD can be retrieved with errors from 1 –
289 6.5×10^{-4} depending on viewing geometry, as shown in Fig. 5. The POD retrieval
290 errors are smaller at longer slant paths and smaller AZAs where the scattering is stronger
291 and sensitivity becomes larger. As we mentioned in Sect. 2.2 the typical AZA for OMI
292 PMC detection varies from 40° to 130° ($\text{SZA} > 35^\circ$, latitude $> 55^\circ\text{N/S}$) and thereby the
293 errors of OMI POD retrievals are expected to have significant dependence on the
294 scattering angle.

295 Figure 6 shows the impact of PMCs on ozone profile retrievals due to the neglect of
296 PMCs, estimated as $\frac{\partial \widehat{x_{O_3}}}{\partial Y} \cdot \frac{\partial Y}{x_{POD}} \cdot \Delta POD$. This result is generally consistent with the effect
297 of PMCs on the OMI and MLS comparisons shown in Figs 1-2: The presence of PMCs
298 results in negative ozone retrieval errors above 6 hPa, the ozone errors increase rapidly
299 up to ~ 0.5 hPa and continue to increase with the greatest peak impact at 0.2 hPa (60 km).
300 At $\text{AZA} = 135^\circ$ (Fig. 6.a) ozone errors increase -2.5% for POD of 10^{-4} to -25% for
301 POD of 10^{-3} . These ozone retrieval errors are expected to increase at longer slant paths
302 and smaller AZAs. For example, as shown in Fig. 6.b, the errors increase by a factor of 5
303 when the AZA is changed to 45° .

304 **3.3 Simultaneous retrievals of ozone profile and PMC optical** 305 **depth**

306 As mentioned in Sect. 2.3, the POD a priori value and its error are determined as
307 0 and 10^{-3} , respectively, by trial and error. The POD initial value of 10^{-4} is close to the
308 minimum value that is detectable from UV radiances below 300 nm as shown in Figs. 4.
309 a and b. An example for POD retrieved from OMI nadir measurements with three a priori
310 errors is presented in Fig. 7. This example illustrates that the a priori error value of



311 10^{-4} is a very tight constraint as the retrieved POD values are very small for both PMC
312 and non-PMC pixels. This also indicates that the POD can be consistently retrieved from
313 measurement information with a priori error values $\geq 10^{-3}$, implying that the degree of
314 freedom for signal is close to 1 for the POD parameter. The retrieved optical depths are
315 generally larger at PMC pixels than at non-PMC pixels. Furthermore, the significant
316 correlation ($r \sim 0.8$) between POD and albedo residuals is demonstrated in Fig. 8. The
317 typical value of the retrieved optical depth is around $1 - 5 \times 10^{-4}$ and increases up to
318 15×10^{-4} for bright PMC pixels. We select the a priori error of POD as 10^{-3} that is
319 closer to the maximum of retrieved POD values. Solution errors for PMC increase
320 from 1×10^{-4} at larger SZAs to 4×10^{-4} at smaller SZAs. These retrieval errors are
321 distinctly smaller than the a priori error of 10^{-3} . This result are consistent with the
322 sensitivity studies as shown in Fig. 5, considering the AZAs for OMI measurements used
323 in Fig. 7 vary from 61° and 89° and VZAs are within 11° .

324 Figure 8b compares the retrieved ozone columns above 40 km with and without
325 including the POD in the state vector. It illustrates that the retrieved ozone values tend to
326 be larger if the PODs are simultaneously retrieved because of positive correlations
327 between POD and ozone parameters in the upper atmosphere; the POD parameter has the
328 most noticeable correlations ($R = 0.4-0.8$) with ozone in the layers of 0.087-3.96 hPa and
329 weak correlations ($R < 0.2$) with other fitting parameters. The ozone column differences
330 are larger for PMC pixels than for non-PMC pixels, indicating that the simultaneously
331 retrieved POD could correct the negative biases in OMI ozone retrievals. However, there
332 are non-PMC pixels that show significant correlation between the POD and ozone
333 parameters at SZAs $57^\circ-67^\circ$, indicating that some PMC pixels are not detected from OMI.
334 Figure 9 and 10 evaluate the improvements of OMI/MLS ozone profile comparisons with
335 the simultaneous retrievals of POD and ozone. The systematic biases due to PMCs are
336 mostly corrected, especially for bright PMC pixels: the negative biases range from 15%
337 to 50% depending on the PMC albedo residuals in the upper atmosphere, but are reduced



338 from $\pm 5\%$ to $\pm 15\%$. The significant negative correlation between OMI/MLS ozone
339 differences and PMC albedo residuals found in Figure 3 is reduced to within 0.1 in most
340 layers, except for the topmost two layers ($R=-0.25$). However, the simultaneous
341 ozone/POD retrievals systematically show positive biases ($\sim 10\%$) for the layers of 1.21-
342 2.15 hPa relative to MLS data, irrespective of albedo residuals, and even for non-PMC
343 pixels. These biases indicate that there are positive signals of fitting residuals induced by
344 not PMC scatterings, but other errors (instrument errors, forward model errors, and other
345 unknown errors), which are misinterpreted to PMC scatterings.

346 4. Summary and Discussion

347 This work demonstrates the interference of tenuous PMCs on OMI ozone profile
348 retrievals above 6 hPa. The presence of PMCs leads to the systematic biases of -2% at 2
349 hPa and -20% at 0.5 hPa for pixels with PMCs in both hemispheres; however, the overall
350 impact on the average ozone in the NH are three times larger than that in the SH if the
351 PMC occurrence frequency is considered. The magnitude of systematic biases can
352 increase to up to $\sim 60 - 80\%$ for very bright PMC pixels. Despite the large relative biases
353 in the upper atmosphere, the impact of PMCs on our retrieved total ozone (~ 305 DU for
354 the NH summer polar region) is negligible with the absolute biases of ~ 0.05 DU at 0.5
355 hPa.

356 Sensitivity analysis shows that the PMC sensitivity is strongly dependent on
357 wavelength, larger at shorter wavelengths where the signals are weak. PMC sensitivity is
358 also strongly dependent on viewing geometry in the forward scattering direction (e.g.,
359 relative azimuth angles less than 90°); PMC sensitivity increases with larger SZAs and
360 VZAs due to longer path lengths for PMC scattering and especially with smaller AZAs
361 due to much stronger forward scattering. For AZAs greater than 90° , the dependence
362 becomes insignificant because the PMC scattering varies much less with viewing
363 geometry. PMC optical depth of $\sim 10^{-4}$ is detectable from OMI data in the back



364 scattering direction and the PMC detection limit could be smaller for the forward
365 scattering direction. The maximum contribution of ignoring PMC to ozone retrievals is
366 found at ~ 0.2 hPa.

367 To reduce PMC interference on upper level ozone retrievals, we added the PMC
368 optical depth (POD) to the state vector in the OMI optimal estimation ozone profile
369 algorithm. The PMC a priori value and a priori error are set at 0 and 10^{-3} , respectively in
370 this study. The selected a priori error value corresponds to a loose constraint, implying
371 that the retrieved optical depth comes mainly from measurement information. As a result,
372 the POD can be retrieved with uncertainties of $1 - 4 \times 10^{-4}$ depending on solar zenith
373 angle. A near-linear relationship is found between POD and albedo residuals ($R \sim 0.8$); the
374 retrieved POD values are $1 - 5 \times 10^{-4}$ at dark PMC pixels and increase up to
375 15×10^{-4} for bright PMC pixels. We finally demonstrated that the simultaneous
376 retrieval of POD could improve the OMI and MLS comparisons. The negative OMI
377 biases of 15-50% are reduced to within $\pm 15\%$ after simultaneous ozone/POD retrievals.
378 Moreover, this simultaneous retrieval reduces the strong negative correlation between
379 OMI/MLS biases and PMC albedo residuals to ~ 0.1 above 2 hPa, which is found to be
380 stronger than -0.5 for ozone retrieval only. However, there are some non-PMC pixels
381 where large POD values are retrieved and hence are correlated with ozone parameters,
382 which might represent undetected PMC pixels from OMI UV measurements. In addition,
383 simultaneous ozone/POD retrievals cause systematic positive biases of $\sim 10\%$ relative to
384 MLS for the layers of 1.21-2.15 hPa, even at non-PMC pixels. It might be explained that
385 positive signal of fitting residuals induced by other factors are misinterpreted to PMC
386 scatterings.

387 This study indicates that the impact of PMC scattering is likely not negligible for
388 stratospheric ozone retrievals from OMI, SBUV, SBUV/2, GOME, GOME-2,
389 SCIAMACHY, and OMPS Nadir Profiler as the effects of PMCs have not been taken
390 into account in any of the operational ozone profile algorithms. The presence of PMCs



391 has greater influence on our OMI ozone retrievals compared to the PMC-induced errors
392 on SBUV and SBUV/2 ozone retrievals shown in Thomas et al., (1991) and Bhartia et al.
393 (2013), which could be explained by OMI having more chances to see brighter PMC
394 pixels due to its much smaller pixel size and by our algorithm using continuous
395 wavelengths of 270-330 nm whereas the SBUV algorithms use several discrete
396 wavelength bands between 240 and 340 nm. In addition, the different ozone retrieval
397 algorithms have different sensitivity to PMC contamination. For example, PMC-induced
398 errors in Nimbus-7 SBUV ozone data based on the NASA Version 5 algorithm
399 (McPeters et al, 1980) can be as large as 10 %. Recently, Bhartia et al. (2013) did some
400 analysis of PMC effects on NOAA-18 SBUV/2 ozone data using the NASA Version 8.6
401 algorithm and found that the average effects are typically in the 2-3% range. Likewise,
402 the OMI operational ozone profile product, OMO3PR (Kroon et al., 2011) has different
403 response to PMC contamination due to different implementation details although it is
404 also based on optimal estimation with the same fitting window; the comparison between
405 two OMI algorithms has been described in Bak et al., (2015). We compare the OMO3PR
406 ozone product between PMC and non-PMC pixels, similarly to Fig. 1.a (not shown here).
407 The impact of PMCs on the OMO3PR product is comparable to our ozone retrievals
408 below 0.1 hPa, but becomes smaller above them with erroneous ozone reduction of ~ 10%
409 at 0.5 hPa. This smaller impact is likely due to fitting of second-order polynomial
410 radiance offsets to account for stray lights [Personal communication, P. Veefkind], which
411 is not used in our algorithm. The impact of PMCs on total ozone retrievals such as
412 OMTO3 (Bhartia and Wellemeyer, 2002) and OMDOAO3 (Veefkind et al., 2006) are
413 negligible because the total ozone algorithms use longer wavelengths than 310 nm where
414 the PMC signal is very weak and the impacts of PMCs on the ozone columns are too
415 small to affect the total ozone retrievals.

416

417 **Acknowledgements** The authors thank the OMI and MLS science teams for providing



418 the satellite data. Research at Pusan National University by J. Bak and J.H. Kim was
419 finally supported by the 『2016 Post-Doc. Development Program』 of Pusan National
420 University and the Eco Innovation Program of KEITI (2012000160002), South Korea.
421 Research at the Smithsonian Astrophysical Observatory by X. Liu, and K. Chance, as
422 well as J. Bak during her 3-month visit to Harvard-Smithsonian was funded by NASA
423 Aura science team program (NNX11AE95G and NNX14AF16G) and the Smithsonian
424 Institution.

425 References

- 426 Bailey, S. M., Merkel, A. W., Thomas, G. E., and Carstens, J. N.: Observations of polar
427 mesospheric clouds by the Student Nitric Oxide Explorer, *J. Geophys. Res.*, 110, D13203,
428 doi:10.1029/2004JD005422, 2005.
- 429 Bak, J., Liu, X., Kim, J. H., Chance, K., and Haffner, D. P.: Validation of OMI total ozone
430 retrievals from the SAO ozone profile algorithm and three operational algorithms with
431 Brewer measurements, *Atmos. Chem. Phys.*, 15, 667-683, doi:10.5194/acp-15-667-2015,
432 2015.
- 433 Baumgarten, G. and Thomas, G. E.: The importance of ice particle shape on UV measurements of
434 polar mesospheric clouds: SBUV/2 observations, *J. Atmos. Sol. Terr. Phys.*, 68(1), 78 – 84,
435 doi:10.1016/j.jastp.2005.08.007, 2006.
- 436 Bhartia, P. K. and Wellemeyer, C.: TOMS-V8 total O3 algorithm, in OMI Algorithm Theoretical
437 Basis Document, vol. II, OMI Ozone Products, ATBD-OMI-02, edited by P. K. Bhartia,
438 pp. 15matology (vs. 20% Space Flight Cent., Greenbelt, Md., available at http://eospsospace.nasa.gov/eos_homepage/for_scientists/atbd/index.php, 2002.
- 440 Bhartia, P. K., McPeters, R. D., Flynn, L. E., Taylor, S., Kramarova, N. A., Frith, S., Fisher, B.,
441 and DeLand, M.: Solar Backscatter UV (SBUV) total ozone and profile algorithm, *Atmos.*
442 *Meas. Tech.*, 6, 2533-2548, doi:10.5194/amt-6-2533-2013, 2013.
- 443 DeLand, M. T., Shettle, E. P., Thomas, G. E., and Olivero, J. J.: Solar backscattered ultraviolet
444 (SBUV) observations of polar mesospheric clouds (PMCs) over two solar cycles, *J.*



- 445 Geophys. Res., 108, 8445, doi: 10.1029/2002JD002398, 2003.
- 446 DeLand, M. T., Shettle, E. P, Thomas, G. E., and Olivero, J. J.: A quarter-century of satellite PMC
447 observations, *J. Atmos. Sol. Terr. Phys.*, 68, 9–29, doi:10.1016/j.jastp.2005.08.003, 2006.
- 448 DeLand, M. T., Shettle, E. P, Thomas, G. E., and Olivero, J. J.: Latitude-dependent long-term
449 variations in polar mesospheric clouds from SBUV version 3 PMC data, *J. Geophys. Res.*,
450 112, D10315, doi:10.1029/2006JD007857, 2007.
- 451 DeLand, M. T., Shettle, E. P., Levelt, P. F., and Kowalewski M. G.: Polar Mesospheric Clouds
452 (PMCs) Observed by the Ozone Monitoring Instrument (OMI) on Aura, *J. Geophys. Res.*,
453 115, D21301, doi:10.1029/2009JD013685, 2010.
- 454 DeLand, M. T., Shettle, E. P, Thomas, G. E., and Olivero, J. J.: Direct observations of PMC local
455 time variations by Aura OMI, *J. Atmos. Sol. Terr. Phys.*, 73, 2049–2064,
456 doi:10.1016/j.jastp.2010.11.019, 2011.
- 457 DeLand, M. T., and Thomas, G. E.: Updated PMC trends derived from SBUV data, *J. Geophys.*
458 *Res. Atmos.*, 120, doi:10.1002/2014JD022253, 2015.
- 459 Englert, C. R., and Stevens, M. H.: Polar mesospheric cloud mass and the ice budget: 1.
460 Quantitative interpretation of mid-UV cloud brightness observations, *J. Geophys. Res.*, 112,
461 08204, doi: 10.1029/2006JD007533, 2007.
- 462 Eremenko, M. N., Petelina, S. V., Zasetsky, A. Y., Karlsson, B. , Rinsland, C. P., Llewellyn, E. J.,
463 and Sloan, J. J.: Shape and composition of PMC particles derived from satellite remote
464 sensing measurements, *Geophys. Res. Lett.*, 32, L16S06, doi:10.1029/2005GL023013, 2005.
- 465 European Space Agency (ESA): The GOME Users Manual, ESA Publ. SP-1182, Publ. Div., Eur.
466 Space Res. and Technol. Cent., Noordwijk, Netherlands, 1995.
- 467 Flynn, L., Long, C., Wu, X., Evans, R., Beck, C. T., Petropavlovskikh, I., McConville, G., Yu, W.,
468 Zhang, Z., Niu, J., Beach, E., Hao, Y., Pan, C., Sen, B., Novicki, M., Zhou, S., and Seftor, C. :
469 Performance of the Ozone Mapping and Profiler Suite (OMPS) products, *J. Geophys. Res.*
470 *Atmos.*, 119, 6181–6195, doi:10.1002/2013JD020467, 2014.
- 471 Hervig, M., Thompson, R. E., McHugh, M., Gordley, L. L., Russell III, J. M., and Summers , M.
472 E.: First confirmation that water ice is the primary component of polar mesospheric
473 clouds, *Geophys. Res. Lett.*, 28, 971–974, 2001.



- 474 Hervig, M. E., Gordley, L. L., Stevens, M. H., Russell III, J. M., Bailey, S. M., and Baumgarten,
475 G.: Interpretation of SOFIE PMC measurements: Cloud identification and derivation of
476 mass density, particle shape, and particle size, *J. Atmos. Solar Terr. Phys.*, 71, 316-330,
477 2009.
- 478 Hervig, M. E. and Stevens, M. H.: Interpreting the 35 year SBUV PMC record with SOFIE
479 observations, *J. Geophys. Res. Atmos.*, 119, 12,689–12,705, doi:10.1002/2014JD021923,
480 2014.
- 481 Kroon, M., de Haan, J. F., Veefkind, J. P., Froidevaux, L., Wang, R., Kivi, R., and Hakkarainen, J. J.:
482 Validation of operational ozone profiles from the Ozone Monitoring Instrument, *J. Geophys.*
483 *Res.*, 116, D18305, doi: 10.1029/2010JD015100, 2011.
- 484 Levelt, P. F., van den Oord, G. H. J., Dobber, M. R., Malkki, A., Visser, H., de Vries, J., Stammes, P.,
485 Lundell, J. O. V., and Saari, H.: The Ozone Monitoring Instrument, *IEEE Trans. Geosci.*
486 *Remote Sens.*, 44(5), 1093–1101, doi:10.1109/TGRS.2006.872333, 2006.
- 487 Liu, X., Bhartia, P.K, Chance, K, Spurr, R.J.D., and Kurosu, T.P.: Ozone profile retrievals from the
488 ozone monitoring instrument, *Atmos. Chem. Phys.*, 10, 2521-2537, doi:10.5194/acp-10-
489 2521-2010, 2010a.
- 490 Liu, X., Bhartia, P. K., Chance, K., Froidevaux, L., Spurr, R. J. D., and Kurosu, T. P.: Validation of
491 Ozone Monitoring Instrument (OMI) ozone profiles and stratospheric ozone columns with
492 Microwave Limb Sounder (MLS) measurements, *Atmos. Chem. Phys.*, 10, 2539-2549,
493 doi:10.5194/acp-10-2539-2010, 2010b.
- 494 Livesey, N. J., Read, W. G., Wagner, P. A., Froidevaux, L., Lambert, A., Manney, G. L., Mill'an
495 Valle, L. F., Pumphrey, H. C., Santee, M. L., Schwartz, M. J., Wang, S., Fuller, R. A.,
496 Jamot, R. F., Knosp, B. W., Martinez, E.: Version 4.2x Level 2 data quality and
497 description document, JPL California Institute of Technology, Pasadena, California,
498 91109–8099,2015.
- 499 Lumpe, J. D., Bailey, S. M., Carstens, J. N., Randall, C. E., Rusch, D. W., Thomas, G. E., Nielsen,
500 K., Jeppesen, C., McClintock, W. E., Merkel, A. W., Riesberg, L., Templeman, B.,
501 Baumgarten, G., and Russell III, J. M.: Retrieval of polar mesospheric cloud properties
502 from CIPS: Algorithm description, error analysis and cloud detection sensitivity, *J. Atmos.*



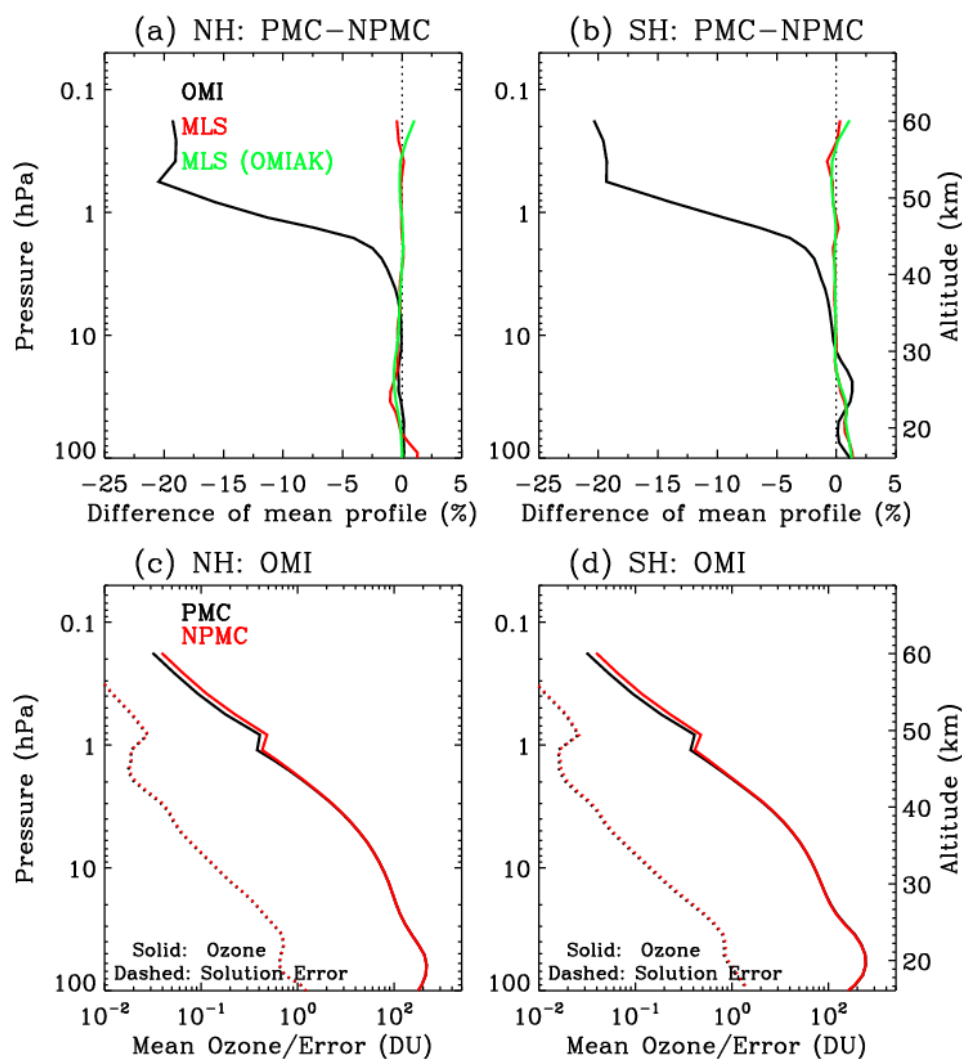
- 503 Solar-Terr. Phys., 104, 167-196, 2013.
- 504 McPeters, R. D.: The Behavior of Ozone near the Stratopause from 2 Years of BUUV Observations,
505 J. Geophys. Res.-Oc. Atm., 85, 4545–4550, 1980.
- 506 McPeters, R. D. and Labow, G. J.: Climatology 2011: an MLS and sonde derived ozone
507 climatology for satellite retrieval algorithms, J. Geophys. Res., 1117, 10303,
508 doi:10.1029/2011JD017006, 2012.
- 509 Munro, R., Eisinger, M., Anderson, C., Callies, J. , Corpaccioli, E. , Lang, R., Lefebvre, A.,
510 Livschitz, Y., and Pérez Albiñana, A. : GOME-2 on MetOp, paper presented at the 2006
511 EUMETSAT Meteorological Satellite Conference, Eur. Org. for the Exploit. of Meteorol.
512 Satell., Helsinki, 2006.
- 513 Rapp, M., Thomas, G. E., and Baumgarten, G.: Spectral properties of mesospheric ice clouds:
514 Evidence for nonspherical particles, J. Geophys. Res., 112, D03211,
515 doi:10.1029/2006JD007322, 2007.
- 516 Rodgers, C. D.: Inverse Methods for Atmospheric Sounding: Theory and Practice, World
517 Scientific Publishing, Singapore, 2000.
- 518 Olivero, J. J., and Thomas, G. E.: Climatology of polar mesospheric clouds, J. Atmos. Sci., 43,
519 1263– 1274, 1986.
- 520 Shettle, E. P, DeLand, M. T., Thomas, G. E., and Olivero, J. J.: Long term variations in the
521 frequency of polar mesospheric clouds in the Northern Hemisphere from SBUV, Geophys.
522 Res. Lett., 36, 02803, doi: 10.1029/2008GL036048. 2009.
- 523 Schoeberl, M.R.; Douglass, A.R.; Hilsenrath, E.; Bhartia, P.K.; Beer, R.; Waters, J.W.; Gunson,
524 M.R.; Froidevaux, L.; Gille, J.C.; Barnett, J.J.; Levelt, P.F.; DeCola, P.: Overview of the EOS
525 aura mission, IEEE Transactions on Geoscience and Remote Sensing, 44(5), 1066-1074,
526 doi: 10.1109/TGRS.2005.861950, 2006.
- 527 Spurr, R. J. D.: VLIDORT: A linearized pseudo-spherical vector discrete ordinate radiative transfer
528 code for forward model and retrieval studies in multilayer multiple scattering media, J. Quant.
529 Spectrosc. Ra., 102, 316–342, 2006.



- 530 Spurr, R. J. D.: Linearized pseudo-spherical scalar and vector discrete ordinate radiative transfer
531 models for use in remote sensing retrieval problems, in: Light Scattering Reviews, edited by:
532 Kokhanovsky, A., Springer, New York, 2008.
- 533 Taylor, M. J., Gadsden, M., Lowe, R. P., Zalcik, M. S., and Brausch, J.: Mesospheric cloud
534 observations at unusually low latitudes, *J. Atmos. Solar Terr. Phys.*, 64, 991-999, 2002.
- 535 Thomas, G.E.: Solar mesosphere explorer measurements of polar mesospheric clouds (noctilucent
536 clouds). *Journal of Atmospheric and Terrestrial Physics*, 46, 819–824, doi:10.1016/0021-
537 9169(84)90062-X, 1984.
- 538 Thomas, G. E., McPeters, R. D. and Jensen, E. J.: Satellite observations of polar mesospheric
539 clouds by the solar backscattered ultraviolet spectral radiometer - Evidence of a solar cycle
540 dependence, *J. Geophys. Res.*, 96, 927-939, 1991.
- 541 von Savigny, C., Kokhanovsky, A., Bovensmann, H., Eichmann, K.-U., Kaiser, J., Noel, S.,
542 Rozanov, A. V., Skupin, J., and Burrows, J. P.: NLC detection and particle size determination:
543 first results from SCIAMACHY on Envisat, *Adv. Space Res.*, 34, 851-856, 2004.
- 544 von Savigny, C., and Burrows, J. P.: Latitude variation of NLC particle radii derived from northern
545 hemisphere SCIAMACHY/Envisat limb measurements, *Adv. Space Res.*, 40, 765-771, 2007.
- 546 Veefkind, J. P., De Haan, J. F., Brinksma, E. J., Kroon, M., and Levelt, P. F.: Total ozone from the
547 ozone monitoring instrument (OMI) using the DOAS technique, *IEEE Trans. Geosci. Remote*
548 *Sens.*, 44(5), 1239-1244, doi: 10.1109/TGRS.2006.871204, 2006.
- 549 Warren, S., G.: Optical constants of ice from the ultraviolet to the microwave, *Applied Optics*, Vol.
550 23, Issue 8, pp. 1206-1225, <http://dx.doi.org/10.1364/AO.23.001206>, 1984
- 551 Waters, J.W.; Froidevaux, L.; Harwood, R.S.; Jarnot, R.F.; Pickett, H.M.; Read, W.G.; Siegel, P.H.;
552 Cofield, R.E.; Filipiak, M.J.; Flower, D.A.; Holden, J.R.; Lau, G.K.; Livesey, N.J.;
553 Manney, G.L.; Pumphrey, H.C.; Santee, M.L.; Wu, D.L.; Cuddy, D.T.; Lay, R.R.; Loo,
554 M.S.; Perun, V.S.; Schwartz, M.J.; Stek, P.C.; Thurstans, R.P.; Boyles, M.A.; Chandra,
555 K.M.; Chavez, M.C.; Gun-Shing Chen; Chudasama, B.V.; Dodge, R.; Fuller, R.A.; Girard,
556 M.A.; Jiang, J.H.; Yibo Jiang; Knosp, B.W.; LaBelle, R.C.; Lam, J.C.; Lee, K.A.; Miller,
557 D.; Oswald, J.E.; Patel, N.C.; Pukala, D.M.; Quintero, O.; Scaff, D.M.; Van Snyder, W.;
558 Tope, M.C.; Wagner, P.A.; Walch, M.J., “The Earth observing system microwave limb



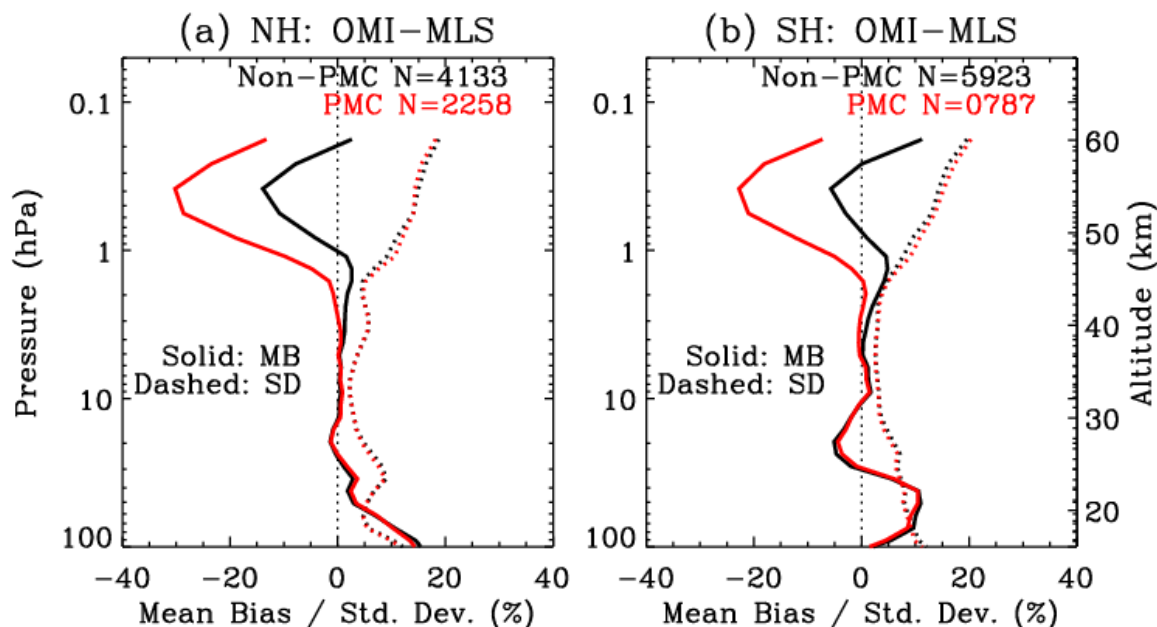
559 sounder (EOS MLS) on the aura Satellite,” in Geoscience and Remote Sensing, IEEE
560 Transactions on , vol.44, no.5, pp.1075-1092, May 2006, doi:
561 10.1109/TGRS.2006.873771, 2006.
562
563
564
565
566
567
568
569
570
571
572
573



574

575 **Figure 1.** Difference of mean ozone profiles from OMI (black), collocated MLS (red),
 576 and MLS convolved with OMI averaging kernels (green) between PMC and non-PMC
 577 pixels ($(\text{PMC} - \text{NPMC})/\text{NPMC} \times 100$ %) (upper panels), with OMI ozone (solid lines)
 578 and solution error (dashed line) profiles averaged over PMC and non-PMC pixels,
 579 respectively (lower panels). (a, c) and (b, d) are results from NH 2007 (July 2007, 75°N-
 580 85°N) and SH 2008 (January 2008, 75°S-85°S) summer seasons, respectively.

581



582

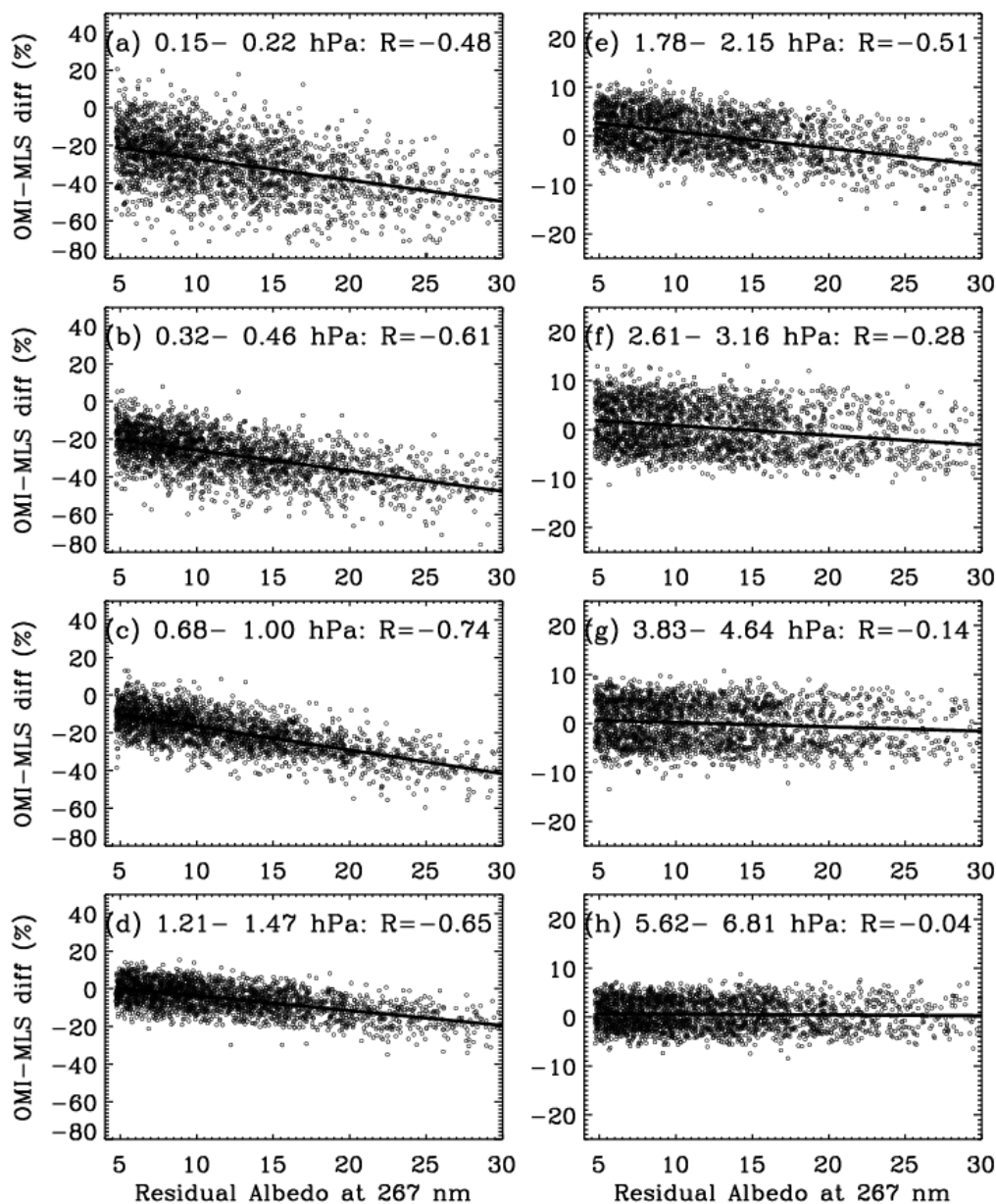
583

584

585

586

Figure 2. Same as Figure 1, but for the mean differences (solid lines) between OMI and collocated MLS convolved with OMI averaging kernels, $(\text{OMI-MLS})/\text{OMI a priori} \times 100\%$, and their 1σ standard deviations (dashed lines) for PMC (red) and non-PMC (black) pixels. The number of collocations (N) is shown in the legend.



587

588 **Figure 3.** Scatter plots between OMI/convolved MLS partial column ozone difference
589 (%) for eight MLS layers and PMC albedo residual at 267 nm ($\times 10^{-6} \text{ sr}^{-1}$) for NH 2007
590 summer, with the linear regression line. The correlation coefficients (R) are shown in the
591 legend.



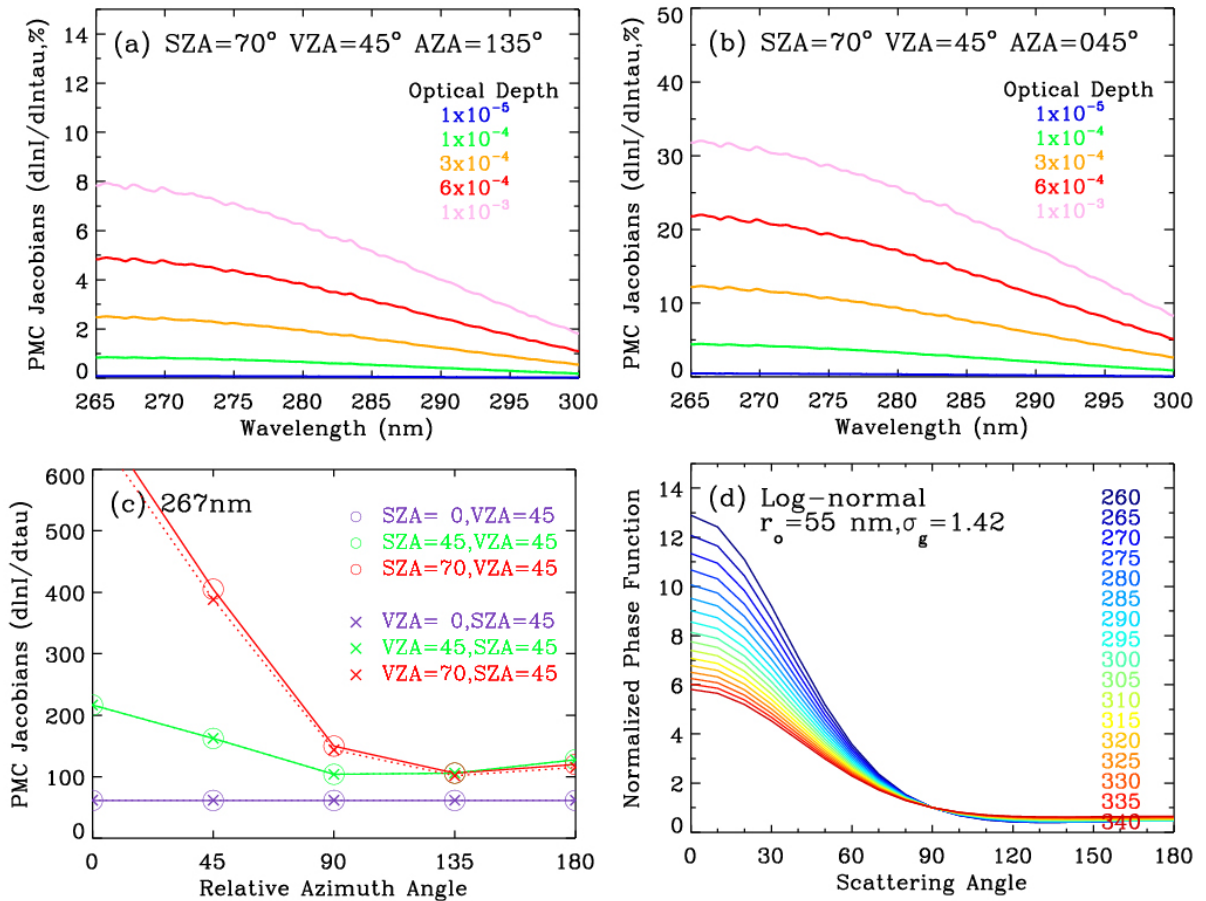
592

593 **Table 1.** Correlation between OMI/convolved MLS ozone differences and PMC albedo
594 residuals at 267nm as shown in Figure 3, but for SH 2008 summer.

Layer (hPa)	Correlation	Layer (hPa)	Correlation
0.15-0.22	-0.42	1.78-2.15	-0.48
0.32-0.46	-0.57	2.61-3.16	-0.35
0.68-1.00	-0.59	3.83-4.64	-0.26
1.21-1.47	-0.54	5.62-6.81	-0.14

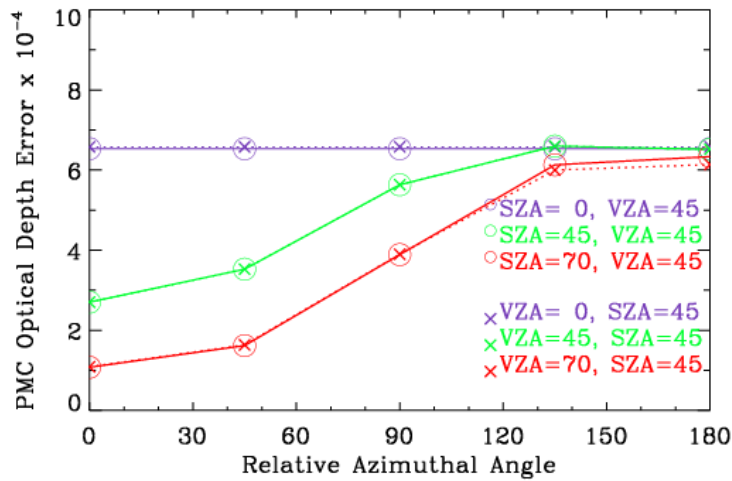


595
 596
 597



598
 599
 600
 601
 602
 603
 604
 605

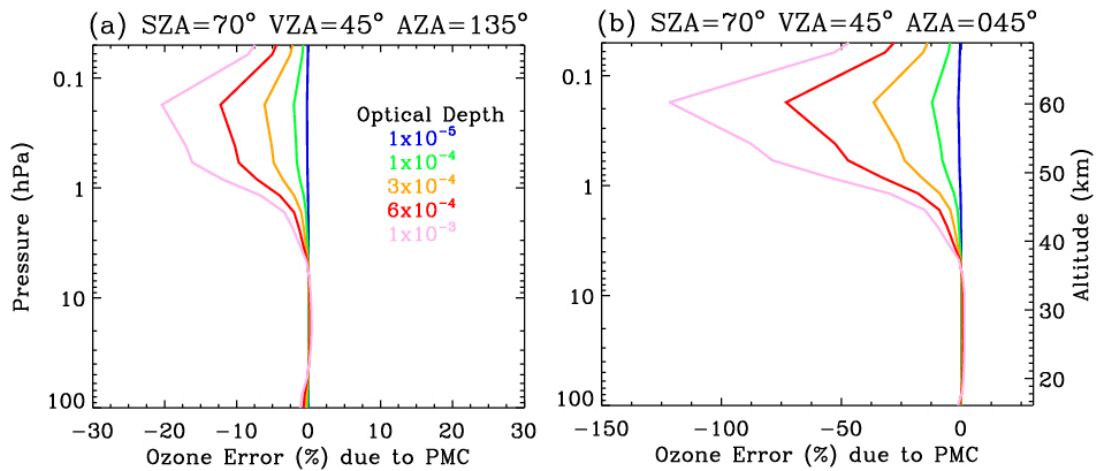
Figure 4. (a) Jacobians with respect to PMC optical depth (“tau”) as functions of wavelength at SZA =70°, VZA= 45°, and AZA=135° for five optical depth values ranging from 10^{-5} to 10^{-3} . (b) Same as (a), but for AZA=45°. (c) Normalized PMC Jacobians at 267 nm as a function of AZA with various SZAs and VZAs. (d) PMC phase function as a function of scattering angle (Φ) for wavelengths ranging from 260 to 340 nm, normalized to unity at $\Phi = 90^\circ$.



606

607 **Figure 5.** Same as Fig. 4.c, but for PMC optical depth retrieval errors (root sum square of
 608 random noise and smoothing errors).

609



610

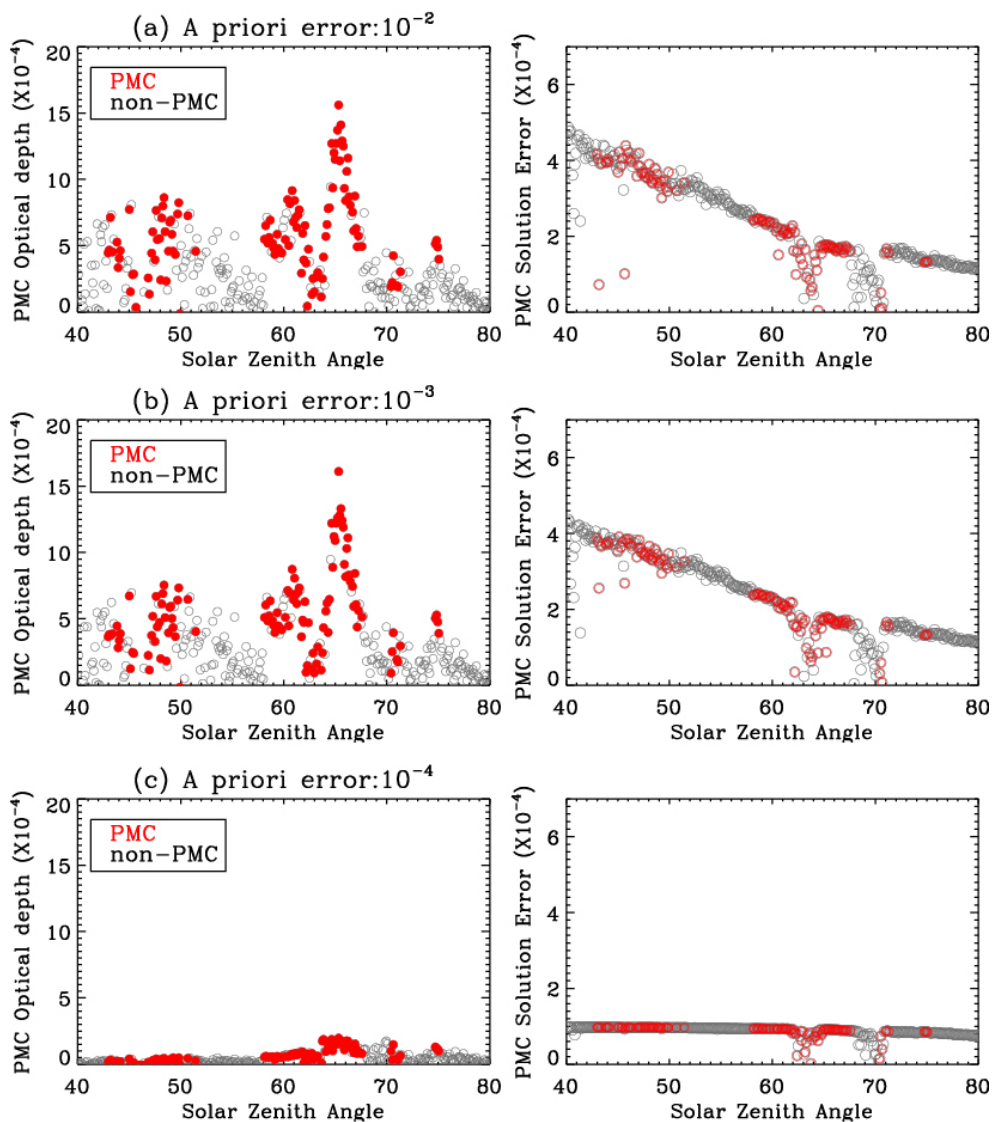
611 **Figure 6.** Ozone profile retrieval errors as functions of pressure due to the neglect of
 612 PMCs estimated based on the optimal estimation approach.

613

614

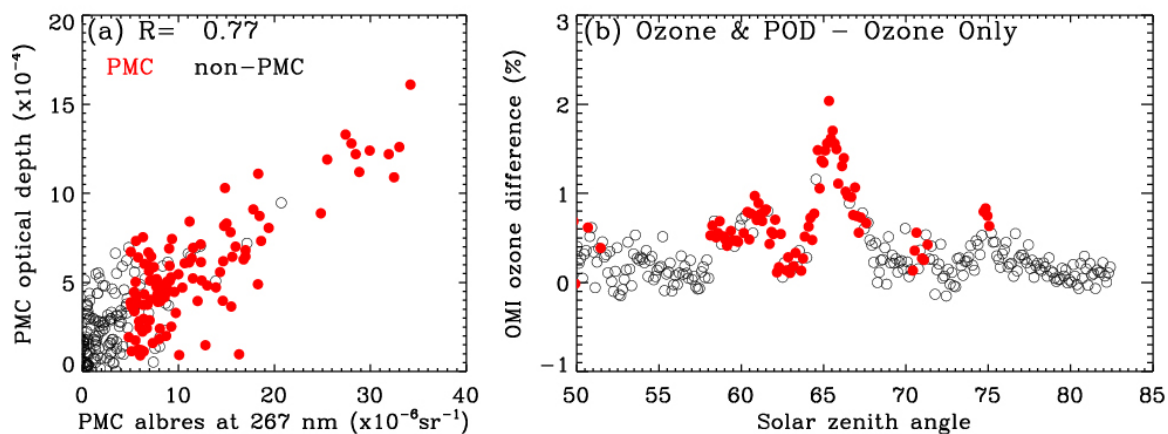
615

616



617

618 **Figure 7.** Retrieved PMC optical depth values and retrieval errors as functions of solar
619 zenith angle for OMI orbit number 15881 and cross-track position 13 (UV1) with a fixed
620 a priori value of 0 and three a priori error values, (a) 10^{-2} , (b) 10^{-3} , and (c) 10^{-4} ,
621 respectively.



622

623 Figure 8. (a) Scatter plot between retrieved PMC optical depths (POD) and PMC albedo
624 residuals at 267 nm for OMI orbit number 15881 and cross-track position 13 (UV1). (b)
625 OMI ozone column (above 40 km) differences between “Ozone & POD” and “Ozone
626 Only” retrieval modes.

627

628

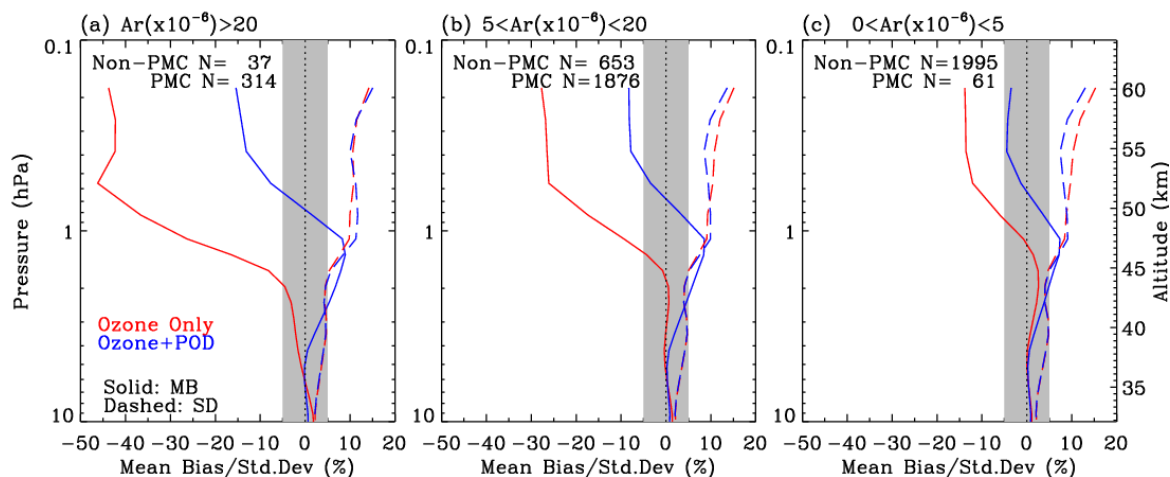
629

630

631

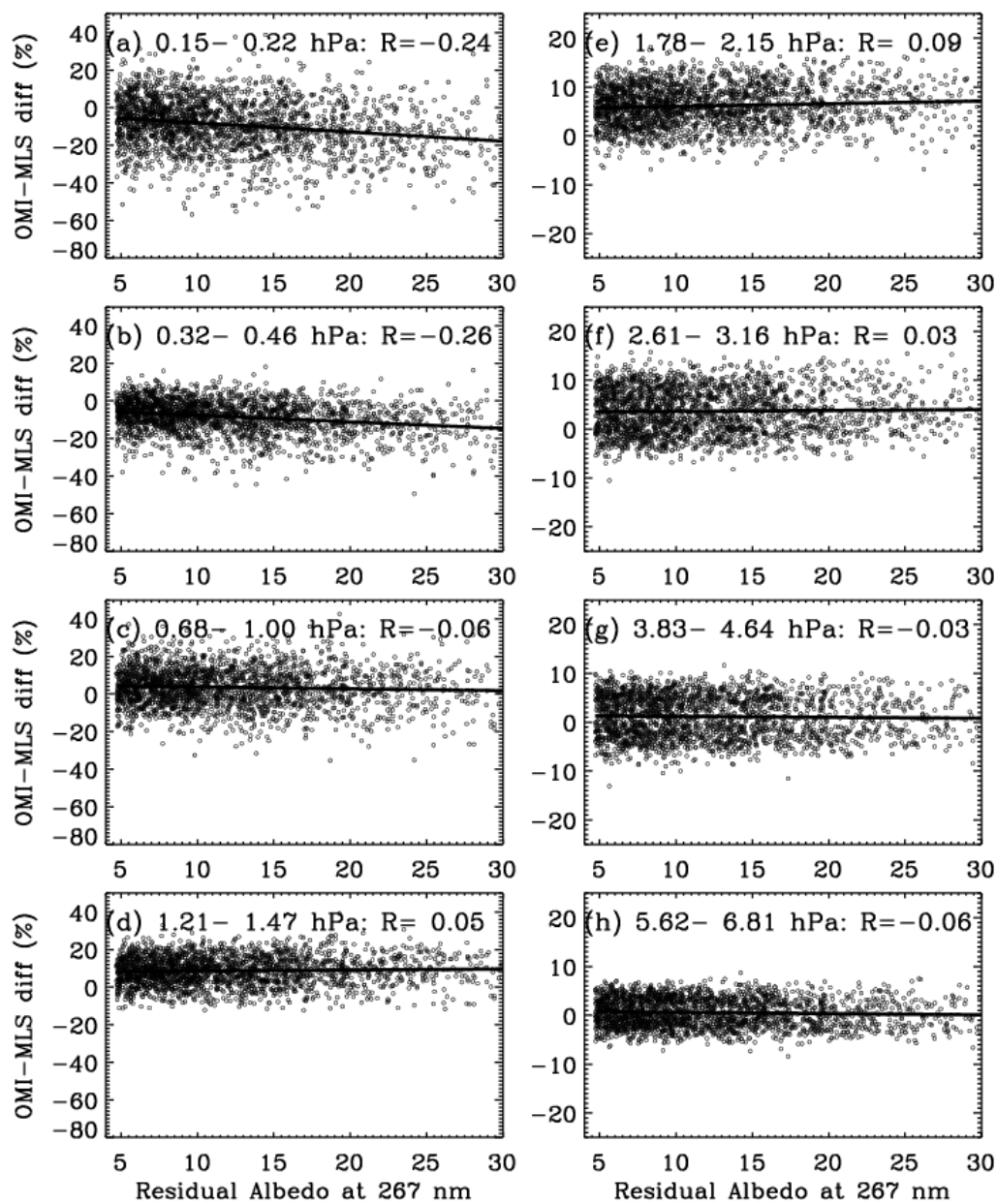
632

633



634

635 **Figure 9.** Collocated OMI/convolved MLS profile differences (solid lines) and their 1σ
636 standard deviations (dashed lines) for different ranges of PMC albedo residual (Ar)
637 values (sr^{-1}) at 267 nm for the NH 2007 summer season. The blue and red lines
638 represent the comparisons when OMI ozone profiles are retrieved with and without PMC
639 optical depths (PODs), respectively. The numbers of the Non-PMC and PMC pixels are
640 included as legends.



641
642
643
644

Figure 10. Same as Figure 3, but with PMC optical depths simultaneously retrieved with ozone.